



Contents lists available at ScienceDirect

International Journal of Solids and Structures

journal homepage: www.elsevier.com/locate/ijsolstr

Damage modeling employing strain gradient continuum theory

Filip Putar, Jurica Sorić*, Tomislav Lesičar, Zdenko Tonković

Faculty of Mechanical Engineering and Naval Architecture, University of Zagreb, Ivana Lučića 5, 10002 Zagreb, Croatia

ARTICLE INFO

Article history:

Received 23 January 2017

Revised 3 April 2017

Available online xxx

Keywords:

Quasi-brittle damage

 C^1 continuity finite element

Strain gradient theory

Heterogeneous material

ABSTRACT

A damage model for quasi-brittle materials embedded into the two dimensional C^1 continuity triangular finite element formulation based on the strain gradient continuum theory is considered. The isotropic damage law is applied to the higher-order stress-strain constitutive model, which enables the analysis of both homogeneous and heterogeneous materials. Such softening formulation also ensures a decrease of the intensity of the material nonlocality associated with the damage growth, which is necessary for the correct description of the narrow localized deformation. In order to obtain the required constitutive matrices, the second-order homogenization procedure is applied to the various representative volume elements in the frame of a multiscale approach. The derived finite element formulation is implemented into the finite element program ABAQUS by means of user subroutines. The superior regularization capabilities, as well as the accuracy and efficiency of the proposed higher-order gradient damage model are demonstrated by the standard benchmark examples.

© 2017 Elsevier Ltd. All rights reserved.

1. Introduction

The damage phenomenon, macroscopically characterized by decrease in the elastic material stiffness or so-called softening, is common in all engineering materials and can significantly decrease structural load-carrying capacity and eventually lead to a complete loss of mechanical integrity. When there is no plasticity involved before or after initiation of damage, materials soften immediately after reaching the critical elastic deformation and can be then classified as quasi-brittle. Materials like these include, among others, high-strength steels, polymers, composites and various geo-materials such as concrete and rock.

Concerning the numerical simulations, it is well-known that the strain softening cannot be properly resolved with the application of the classical continuum mechanics. This approach leads to the local loss of positive definiteness of the material tangent stiffness, which may cause the local loss of ellipticity of the governing differential equations. The mathematical description of the model then becomes ill-posed and numerical solutions do not converge to a physically meaningful solution (Peerlings et al., 1996). If the finite elements are applied as a discretization technique, the solutions are then completely dependent on both mesh refinement and mesh alignment. In other words, the energy dissipated in the fracture process tends to zero when the size of the elements in-

involved in the softening process is reduced, and the localization zone exhibits an extreme tendency to propagate along the mesh lines (de Borst et al., 1993).

Various regularization techniques have been developed in the past few decades to overcome this problem. Many of them are based on the improvement of the classical continuum model, precisely on its enrichment with the internal length scale parameter in several different ways. Some of the known methods include the micropolar (Chang and Ma, 1990) and viscoplastic theory (Sluys and de Borst, 1992), but they suffer from the lack of generality since the preservation of ellipticity is possible only in some specific cases. On the other hand, the theories related to the nonlocal material behavior have been shown to be the most versatile. In the case of the nonlocal models, the stress at a material point does not depend only on the strain and other state variables at this point, as it is the case with the classical continuum theory, but also on the strains and other state variables of the points in the surrounding area. Physically, the nonlocality represents the heterogeneities and interactions taking place at the microscale, which cannot be neglected in the damage analysis, where the scale of the macrostructural fluctuations of the constitutive variables approaches the scale of the microstructure (Bažant, 1991). The intensity of these interactions is described by the aforementioned internal length scale parameter, which in this way introduces a microstructural contribution in the model (Peerlings, 1999).

Basically, there are two different approaches regarding the implementation of the material nonlocality in the model, the integral and the gradient approach. The integral approach, introduced by Bažant et al. (1984), accounts for the influence of previously men-

* Corresponding author.

E-mail addresses: filip.putar@fsb.hr (F. Putar), jurica.soric@fsb.hr (J. Sorić), tomislav.lesicar@fsb.hr (T. Lesičar), zdenko.tonkovic@fsb.hr (Z. Tonković).

tioned microstructural interactions through the weighted average of a variable driving the damage process, typically strain. This leads to very complicated constitutive relations made of convolution-type integrals, making the numerical implementation very demanding. In the case of the gradient approach, either the classical constitutive relation is enhanced with the strain gradients, or both the strain gradients and their stress conjugates are introduced in the model via higher-order continuum. In the case when only strain-gradients are used as an enhancement of the constitutive relation, the explicit and especially the implicit gradient formulations are usually used when dealing with softening, either in elasticity context (Peerlings et al., 1998), plasticity context (de Borst and Mühlhaus, 1992; Engelen et al., 2003) or in the analysis of the elastic wave propagation (Sluys et al., 1993). Although the structural responses are mesh objective, the mentioned formulations suffer from the spurious damage growth reported by Simone et al., (2004), where the damage process zone evolves incorrectly after initiation in the mode-I and the shear band problems. The described phenomenon occurs if the conventional integral and gradient enhancements are used, which assume a constant interaction domain throughout the entire load history. Because of this assumption, the energy is transferred from the damage process zone to a neighboring elastically unloading region, resulting in a smeared damage zone instead in a localized deformation band (Poh and Sun, 2017). This problem can be more or less successfully avoided by using the modified nonlocal formulations which assume the evolving internal length scale parameter. Most of these formulations employ the increasing length scale parameter with the rising deformation level (Pijaudier-Cabot et al., 2004; Nguyen, 2011; Triantafyllou et al., 2015). By doing so, it is presumed that the intensity of microstructural interactions also increases, which does not have a correct physical background. This is explained in more detail in (Poh and Sun, 2017), where a new model based on the decreasing microstructural interactions is presented, recognizing that the width of the fracture process zone localizes towards a macroscopic crack in the quasi-brittle fracture.

The strain gradient continuum theory, where both the strain gradients and their stress conjugates contribute to the internal energy (Mindlin and Eshel, 1968) is employed less often, mainly because it is numerically more complex. In the recent developments, this higher-order stress-strain theory is employed in the context of a damage modeling of an infinitely long bar (Chang et al., 2002), where it is concluded that the addition of the higher-order stress terms results in stabilizing the positive definiteness of the tangent stiffness moduli when entering the strain softening regime. In such a way the physically consistent solutions leading to a realistic reproduction of the softening phenomenon can be ensured. Further development from one-dimensional to multi-dimensional simulation of a localized failure process is made in (Yang and Misra, 2010). In both Chang et al. (2002) and Yang and Misra (2010) element-free Galerkin (EFG) meshless method is used for finding the approximate solutions to the corresponding boundary value problems. Another advantage of the higher-order stress-strain theory is that material heterogeneity in the constitutive relations can be easily introduced through the non-diagonal higher order material stiffness tangents (Kaczmarczyk et al., 2008). The stiffness tangents can be obtained by applying the second-order homogenization technique (Kouznetsova et al., 2002) on the representative volume element (RVE) (Gitman et al., 2007). The constitutive relations emerging from the second-order homogenization described in Kouznetsova et al. (2002) and Lesičar et al. (2014) are dependent on the choice of the RVE size, or in other words, the size effect can be studied by changing the RVE sizes rather than changing the model dimensions. On the other hand, as suggested in Li (2011) and Li and Zhang (2013), the gradient constitutive behavior is a material property, and as such it should not be influ-

enced by the choice of the RVE size, but only by a stochastic aspect of the heterogeneities included in the RVE. For this purpose, a correction that is to be applied on the strain gradient modulus of the sixth order is derived in Li (2011), making the overall constitutive relations more consistent and intrinsic. Although the previously mentioned gradient feature of the constitutive law resulting from the standard homogenization procedure is not as physically appropriate, when a real engineering material is considered, the necessary RVE size can be determined and the unique and consistent strain gradient constitutive relations can be obtained. Another limitation of the standard second-order homogenization is concerned with the microfluctuation field inside the RVE, as it is recognized by Forest and Trinh (2011). Here the authors suggest another approach for its resolution by treating the microfluctuation term in the extended Hill-Mandel condition different from zero, which is exactly the opposite from what is generally used in the standard approach, e.g. as described in Kouznetsova et al. (2002) and Lesičar et al. (2014). Beside the second-order computational homogenization, which can be used for an arbitrary RVE geometry and is the most general in that sense, a constitutive model for the materials with a simple microstructure can be established using an analytical approach, e.g. as described in Zybelle et al. (2008).

Concerning the numerical implementation of the strain gradient continuum theory using the finite element method, both C^0 and C^1 continuous elements have already been employed. Zervos et al. (2009) showed a superior robustness of the C^1 displacement based finite elements over the C^0 elements used with a penalty function approach. In Akarapu and Zbib (2006), the C^1 formulation is used for the crack analysis in the context of the linear elastic fracture mechanics. Fischer et al. (2010) presented an in-depth analysis of the performance of three different C^1 continuous finite elements and additionally made a comparison with the C^1 Natural Element Method. Lesičar et al. (2014) developed a triangular displacement based C^1 finite element and used it in the scope of the multiscale modeling of heterogeneous materials. Regarding the damage mechanics, the C^0 finite elements based on the mixed formulation are mostly used due to their lower complexity, either when the implicit gradient enhancement (Peerlings et al., 1996) or the micromorphic approach (Poh and Sun, 2017) is used as a regularization technique. To the authors' knowledge, the two-dimensional C^1 displacement based finite elements have not yet been employed for the analysis of softening materials. Although the C^1 formulation is considered more complex owing to a relatively high polynomial used for the displacement field approximation, there is no need for the introduction of the additional variables representing the link to the microstructure, e.g. the non-local equivalent strain or the micromorphic variable, which are specific for the C^0 formulations. In that sense, the C^1 displacement based finite elements can be considered more intrinsic as all state variables are calculated in terms of the displacements and their derivatives. Besides, due to the mentioned displacement field approximation using a high polynomial, a much coarser discretization is generally sufficient, compared to the C^0 finite elements.

This contribution is concerned with the development of a damage model based on the strain gradient continuum theory which includes both the strain gradients and their stress conjugates. For this purpose, the C^1 continuity displacement based triangular finite element developed in Lesičar et al. (2014) is employed. Unlike in this reference, here the sequential micro-macro procedure is abandoned, although the terms relating to the micro- and the macrostructural level are preserved. The microstructural contribution is incorporated through the constitutive tensors which are obtained using the second-order computational homogenization, while the softening analysis is performed exclusively on the macroscale model once the constitutive tensors are known. The damage model proposed by Yang and Misra (2010) is adopted,

which has a very attractive property to decrease the intensity of the microstructural interactions while the softening progresses. In this way a physically correct structural response standing behind a fracturing process can be captured, unlike the results obtained using the conventional implicit gradient damage model, where the spurious damage growth can be observed (Geers et al., 1998; Simone et al., 2004). Herein, the isotropic damage law is implemented into the constitutive relations of the strain gradient theory, whereby the constitutive matrices, which describe the intensity of the material nonlocal behavior, are directly decreased by the term involving damage variable. All derived numerical algorithms are embedded into the aforementioned C^1 triangular finite element formulation and implemented into the FE software ABAQUS (Simulia, 2013) using user subroutines. The performance of the proposed formulation is demonstrated by two standard benchmark examples, where both homogeneous and heterogeneous materials are considered. In order to test the effect of the varying nonlocal response, only the academic examples of heterogeneous materials are taken into account. It is shown that the proposed formulation succeeds in achieving a complete regularization of the material failure mathematical model, meaning that mesh independent results with no spurious damage growth can be obtained.

The paper has the following structure. Section 2 briefly discusses the fundamentals of the isotropic continuum damage model and gives the most common relations used in the modeling of quasi-brittle damage. In Section 3 the formulation and numerical implementation of the higher-order stress-strain damage theory into the C^1 continuity finite element is presented. Therein, the continuum damage mechanics is realized in its simplest form through the isotropic damage model. The calculation of the stiffness matrices using the second-order homogenization, as well as the overall calculation scheme of the proposed algorithm are also explained in this section. The algorithm is then numerically tested in Section 4 by using two typical benchmark examples, where both homogeneous and heterogeneous materials are employed. The full regularizing capability of the proposed algorithm is demonstrated through a shear band failure problem, also discussed in Simone et al. (2004). The last section is reserved for some concluding remarks.

2. Continuum damage model

The reduction of the elastic stiffness properties in the isotropic damage model is expressed by the following well known relation

$$\mathbf{C}^{\text{eff}} = (1 - D)\mathbf{C}, \quad (1)$$

where D is a scalar damage variable ranging from zero (undamaged material) to one (fully damaged material), while \mathbf{C}^{eff} and \mathbf{C} are the effective and the elastic stiffness tensors, respectively. The damage state is governed by the monotonically increasing scalar history parameter κ , which can be determined as an average local equivalent scalar measure of the strain ε_{eq} through Kuhn-Tucker relations

$$\kappa \geq 0, \quad \varepsilon_{\text{eq}} - \kappa \leq 0, \quad \dot{\kappa}(\varepsilon_{\text{eq}} - \kappa) = 0. \quad (2)$$

The two different equivalent elastic strain measures are generally used in the context of the softening behavior of a quasi-brittle material. The first one is defined in (Mazars and Pijaudier-Cabot, 1989) as

$$\varepsilon_{\text{eq}} = \sqrt{\sum_{i=1}^3 \langle \varepsilon_i \rangle^2} \quad (3)$$

with ε_i ($i=1, 2, 3$) representing the principal strains. It is clear that, in this case, the equivalent elastic strain measure depends only on the positive principal strains, making it more sensitive to tensile than to compressive strains. On the other hand,

the von Mises equivalent strain measure according to de Vree et al. (1995) and given by

$$\varepsilon_{\text{eq}} = \frac{k-1}{2k(1-2\nu)} I_1 + \frac{1}{2k} \sqrt{\frac{(k-1)^2}{(1-2\nu)^2} I_1^2 - \frac{12k}{(1+\nu)^2} J_2}. \quad (4)$$

includes a parameter k which represents the ratio between uniaxial compressive and tensile strength of the material. For the $k=1$, meaning that both compression and tension influence the equivalent strain measure equally, Eq. (4) results in

$$\varepsilon_{\text{eq}} = \frac{1}{1+\nu} \sqrt{-3J_2}. \quad (5)$$

In above expressions I_1 and J_2 are the first invariant of the strain tensor and the second invariant of the deviatoric strain tensor, respectively.

When it comes to the theoretical considerations of the damage process, the damage evolution governed by the linear softening law (Peerlings, 1999) is usually used

$$D = \begin{cases} \frac{\kappa_u(\kappa - \kappa_0)}{\kappa(\kappa_u - \kappa_0)} & \text{if } \kappa_0 \leq \kappa \leq \kappa_u \\ 1 & \text{if } \kappa > \kappa_u \end{cases}, \quad (6)$$

where κ_0 and κ_u are the material parameters representing the threshold strain at which the damage is initiated, and the strain at which material completely loses its stiffness, respectively. The softening in the real materials is usually nonlinear, where the application of the exponential softening law is the most common (Peerlings, 1999)

$$D = 1 - \frac{\kappa_0}{\kappa} \{1 - \alpha + \alpha \exp[\beta(\kappa_0 - \kappa)]\} \quad \text{if } \kappa > \kappa_0 \quad (7)$$

with α and β as model parameters. As evident from above, the damage-driving state variable is a local equivalent strain, which differs from most gradient-enhanced formulations, where the damage is governed by the nonlocal state variable. In this contribution the nonlocality is incorporated through the strain gradient continuum theory, which is discussed in the following section.

3. Damage algorithm based on strain gradient continuum theory

Herein, derivation of the damage algorithm based on the strain gradient continuum theory is presented. For this purpose, the C^1 continuity triangular finite element developed by Lesičar et al. (2014) is employed. Both the basic strain gradient continuum relations and a brief description of the employed finite element are given for clarity reasons only. Because the calculation of the stiffness matrices for heterogeneous materials requires the application of the second-order homogenization, the most important relations of this method are also shown. Thereafter, the softening analysis procedure employing the derived damage algorithm is explained.

3.1. C^1 continuity triangular finite element

The basic strain gradient continuum relations are given in tensorial notation in Table 1. In the small strain continuum theory the strain tensor $\boldsymbol{\varepsilon}$ is defined as a symmetric part of the displacement gradient field $\nabla \otimes \mathbf{u}$, as shown in Eq. (9). In Eq. (11) $\boldsymbol{\sigma}$ is the Cauchy stress tensor and ${}^3\boldsymbol{\mu}$ stands for the third-order double-stress tensor, representing an energetically conjugate measure to the strain gradient tensor ${}^3\boldsymbol{\eta}$. Variation of the work done by internal forces, is defined by Eq. (12) with ∇^A and D as the surface gradient and normal gradient operators, respectively, while \mathbf{n} represents the unit outward normal to surface A of a body of volume V . In the variation of the external work, Eq. (13), \mathbf{t} and $\boldsymbol{\tau}$ stand for the traction

Table 1
Basic relations of the strain gradient continuum.

The strain gradient is defined as	
${}^3\eta = \nabla \otimes \boldsymbol{\varepsilon}$,	(8)
where	
$\boldsymbol{\varepsilon} = \frac{1}{2}(\nabla \otimes \mathbf{u} + (\nabla \otimes \mathbf{u})^T)$,	(9)
The strain energy density function:	
$W = W(\boldsymbol{\varepsilon}, {}^3\eta)$,	(10)
Variation of the strain energy function:	
$\delta W = \boldsymbol{\sigma} : \delta \boldsymbol{\varepsilon} + {}^3\boldsymbol{\mu} : \delta {}^3\eta$,	(11)
Variation of the internal work:	
$\delta W^{\text{int}} = \int_A \{[\mathbf{n} \cdot (\boldsymbol{\sigma} - (\nabla \cdot {}^3\boldsymbol{\mu})) + (\nabla^A \cdot \mathbf{n}) \otimes \mathbf{n} \cdot (\mathbf{n} \cdot {}^3\boldsymbol{\mu}) - \nabla^A \cdot (\mathbf{n} \cdot {}^3\boldsymbol{\mu})] \cdot \delta \mathbf{u}\} dA - \int_V \{[\nabla \cdot (\boldsymbol{\sigma} - (\nabla \cdot {}^3\boldsymbol{\mu}))] \cdot \delta \mathbf{u}\} dV + \int_A [(\mathbf{n} \cdot {}^3\boldsymbol{\mu} \cdot \mathbf{n}) \cdot (D \otimes (\delta \mathbf{u}))] dA$	(12)
with $\nabla^A = \nabla \cdot (\mathbf{1} - \mathbf{n} \otimes \mathbf{n})$ and $D = \mathbf{n} \cdot \nabla$.	
Variation of the external work:	
$\delta W^{\text{ext}} = \int_A (\mathbf{t} \cdot \delta \mathbf{u}) dA + \int_A [\boldsymbol{\tau} \cdot (D \otimes (\delta \mathbf{u}))] dA$,	
where	
$\mathbf{t} = \mathbf{n} \cdot (\boldsymbol{\sigma} - (\nabla \cdot {}^3\boldsymbol{\mu})) + (\nabla^A \cdot \mathbf{n}) \otimes \mathbf{n} \cdot (\mathbf{n} \cdot {}^3\boldsymbol{\mu}) - \nabla^A \cdot (\mathbf{n} \cdot {}^3\boldsymbol{\mu})$, $\boldsymbol{\tau} = \mathbf{n} \cdot {}^3\boldsymbol{\mu} \cdot \mathbf{n}$.	(14)
The effective stress:	
$\tilde{\boldsymbol{\sigma}} = \boldsymbol{\sigma} - (\nabla \cdot {}^3\boldsymbol{\mu})$,	(15)
The equilibrium equation:	
$\nabla \cdot \tilde{\boldsymbol{\sigma}} = \mathbf{0}$.	(16)

and double surface traction vectors, respectively, with their definitions given in Eq. (14). Equilibrium equation (16) is derived from the principle of virtual work ($\delta W^{\text{int}} = \delta W^{\text{ext}}$), where $\tilde{\boldsymbol{\sigma}}$ represents the effective stress defined by Eq. (15). More detailed information on the strain gradient elasticity can be found in (Mindlin, 1965).

The C^1 continuity plane strain triangular finite element derived by the authors of this contribution in (Lesičar et al., 2014) is shown in Fig. 1. It consists of three nodes and 36 degrees of freedom with the displacement field approximated by the condensed fifth order polynomial. The nodal degrees of freedom are the two displacements and their first- and second-order derivatives with respect to the Cartesian coordinates. The physical interpretation of the mentioned nodal degrees of freedom is comprehensively described in (Lesičar et al., 2017). The derivation of the element equations is obtained employing the principle of virtual work, which can be ex-

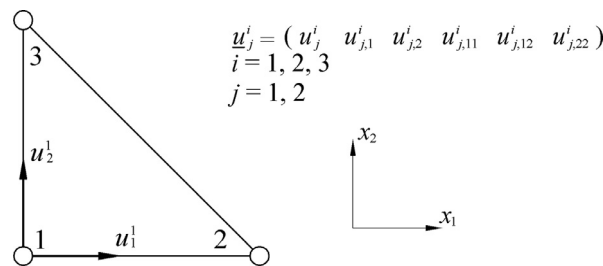


Fig. 1. C^1 triangular finite element (Lesičar et al., 2014).

pressed for the strain gradient continuum as

$$\int_A \delta \boldsymbol{\varepsilon}^T \boldsymbol{\sigma} dA + \int_A \delta \boldsymbol{\eta}^T \boldsymbol{\mu} dA = \int_s \delta \mathbf{u}^T \mathbf{t} ds + \int_s \delta (\text{grad } \mathbf{u}^T) \mathbf{T} ds, \quad (17)$$

with s representing the perimeter of the element and \mathbf{T} the double traction tensor, $\mathbf{T} = \boldsymbol{\tau} \mathbf{n}$. All other quantities are already mentioned and described above. In addition to Eq. (17), the boundary conditions expressed by the displacement and the normal derivative of the displacement ($\nabla \otimes \mathbf{u}) \cdot \mathbf{n}$ should be prescribed to solve the boundary value problem.

The strain and strain gradient tensors are given by

$$\boldsymbol{\varepsilon} = \begin{bmatrix} \varepsilon_{11} \\ \varepsilon_{22} \\ 2\varepsilon_{12} \end{bmatrix} = \mathbf{B}_\varepsilon \mathbf{v}, \quad \boldsymbol{\eta} = \begin{bmatrix} \eta_{111} \\ \eta_{222} \\ \eta_{221} \\ \eta_{112} \\ 2\eta_{121} \\ 2\eta_{212} \end{bmatrix} = \mathbf{B}_\eta \mathbf{v}, \quad (18)$$

where \mathbf{B}_ε and \mathbf{B}_η represent the matrices containing adequate first and second derivatives of the element shape functions \mathbf{N} , while \mathbf{v} is the vector of the nodal degrees of freedom. Considering a non-linear problem described by Eq. (17), the displacement vector \mathbf{u} , the stress tensor $\boldsymbol{\sigma}$ and the double stress $\boldsymbol{\mu}$ are updated according to

$$\begin{aligned} \mathbf{u} &= \mathbf{u}^{i-1} + \Delta \mathbf{u}, \\ \boldsymbol{\sigma} &= \boldsymbol{\sigma}^{i-1} + \Delta \boldsymbol{\sigma}, \\ \boldsymbol{\mu} &= \boldsymbol{\mu}^{i-1} + \Delta \boldsymbol{\mu}, \end{aligned} \quad (19)$$

where the exponent $(i-1)$ refers to the last converged equilibrium state, and the symbol Δ indicates an incremental change and mathematically acts as a differential operator. The incremental constitutive relations for the undamaged material are defined as

$$\Delta \boldsymbol{\sigma} = \mathbf{C}_{\sigma\varepsilon} \Delta \boldsymbol{\varepsilon} + \mathbf{C}_{\sigma\eta} \Delta \boldsymbol{\eta}, \quad (20)$$

$$\Delta \boldsymbol{\mu} = \mathbf{C}_{\mu\varepsilon} \Delta \boldsymbol{\varepsilon} + \mathbf{C}_{\mu\eta} \Delta \boldsymbol{\eta},$$

with $\mathbf{C}_{\sigma\varepsilon}$, $\mathbf{C}_{\sigma\eta}$, $\mathbf{C}_{\mu\varepsilon}$ and $\mathbf{C}_{\mu\eta}$ as the constitutive stiffness matrices. The strain and the second-order strain increments, employing Eq. (18), in terms of the displacement vector increment $\Delta \mathbf{v}$, read

$$\begin{aligned} \Delta \boldsymbol{\varepsilon} &= \mathbf{B}_\varepsilon \Delta \mathbf{v}, \\ \Delta \boldsymbol{\mu} &= \mathbf{B}_\eta \Delta \mathbf{v}. \end{aligned} \quad (21)$$

3.2. Implementation of the isotropic damage law

When the isotropic damage law (1) is applied to the strain gradient constitutive model, the following relations are obtained

$$\begin{aligned} \boldsymbol{\sigma} &= (1 - D) \mathbf{C}_{\sigma\varepsilon} \boldsymbol{\varepsilon} + (1 - D) \mathbf{C}_{\sigma\eta} \boldsymbol{\eta}, \\ \boldsymbol{\mu} &= (1 - D) \mathbf{C}_{\mu\varepsilon} \boldsymbol{\varepsilon} + (1 - D) \mathbf{C}_{\mu\eta} \boldsymbol{\eta}. \end{aligned} \quad (22)$$

Introduction of the damage enhanced constitutive relations represented by Eq. (22) into the principle of the virtual work for the

strain gradient continuum, given by Eq. (17), leads to the following variational expression in terms of the damage variable

$$\begin{aligned} & \int_A \delta \boldsymbol{\varepsilon}^T [(1-D)\mathbf{C}_{\sigma\varepsilon}\boldsymbol{\varepsilon} + (1-D)\mathbf{C}_{\sigma\eta}\boldsymbol{\eta}] dA \\ & + \int_A \delta \boldsymbol{\eta}^T [(1-D)\mathbf{C}_{\mu\varepsilon}\boldsymbol{\varepsilon} + (1-D)\mathbf{C}_{\mu\eta}\boldsymbol{\eta}] dA \\ & = \int_s \delta \mathbf{u}^T \mathbf{t} ds + \int_s \delta (\text{grad } \mathbf{u}^T) \mathbf{T} ds. \end{aligned} \quad (23)$$

In this paper the linearized finite element equation is derived from the principle of the virtual work expressed by Eq. (17), using the standard incremental approach. Accordingly, by inserting Eqs. (19) and (21) into (17), and after some straightforward mathematical manipulation, the following incremental relation may be obtained

$$\begin{aligned} \int_A \mathbf{B}_\varepsilon^T \Delta \boldsymbol{\sigma} dA + \int_A \mathbf{B}_\eta^T \Delta \boldsymbol{\mu} dA & = \int_s (\mathbf{N}^T \mathbf{t} + \text{grad } \mathbf{N}^T \mathbf{T}) ds \\ & - \int_A (\mathbf{B}_\varepsilon^T \boldsymbol{\sigma}^{i-1} + \mathbf{B}_\eta^T \boldsymbol{\mu}^{i-1}) dA. \end{aligned} \quad (24)$$

The right-hand side terms in the above expression represent the external and internal nodal force vectors \mathbf{F}_e and \mathbf{F}_i , respectively. Considering the constant values of the constitutive stiffness matrices and the updates of the strain tensor, the strain gradient tensor and the damage variable in the form of

$$\begin{aligned} \boldsymbol{\varepsilon} & = \boldsymbol{\varepsilon}^{i-1} + \Delta \boldsymbol{\varepsilon}, \\ \boldsymbol{\eta} & = \boldsymbol{\eta}^{i-1} + \Delta \boldsymbol{\eta}, \\ D & = D^{i-1} + \Delta D, \end{aligned} \quad (25)$$

Eq. (22) written in the incremental form reads

$$\begin{aligned} \Delta \boldsymbol{\sigma} & = (1-D^{i-1})(\mathbf{C}_{\sigma\varepsilon} \Delta \boldsymbol{\varepsilon} + \mathbf{C}_{\sigma\eta} \Delta \boldsymbol{\eta}) - \Delta D (\mathbf{C}_{\sigma\varepsilon} \boldsymbol{\varepsilon}^{i-1} + \mathbf{C}_{\sigma\eta} \boldsymbol{\eta}^{i-1}), \\ \Delta \boldsymbol{\mu} & = (1-D^{i-1})(\mathbf{C}_{\mu\varepsilon} \Delta \boldsymbol{\varepsilon} + \mathbf{C}_{\mu\eta} \Delta \boldsymbol{\eta}) - \Delta D (\mathbf{C}_{\mu\varepsilon} \boldsymbol{\varepsilon}^{i-1} + \mathbf{C}_{\mu\eta} \boldsymbol{\eta}^{i-1}). \end{aligned} \quad (26)$$

Here, the incremental change of the damage variable may be expressed by

$$\Delta D = \left(\frac{dD}{d\boldsymbol{\varepsilon}} \right)^{i-1} \Delta \boldsymbol{\varepsilon}, \quad (27)$$

since the damage variable is assumed to be a function only of the strain tensor $D=D(\boldsymbol{\varepsilon})$. When the incremental higher-order damage constitutive model represented by Eq. (26) is embedded into the incremental relation (24), and using Eq. (27), the following expression is obtained

$$\begin{aligned} & \int_A \mathbf{B}_\varepsilon^T \left[(1-D^{i-1})\mathbf{C}_{\sigma\varepsilon}\mathbf{B}_\varepsilon \Delta \mathbf{v} - \mathbf{C}_{\sigma\varepsilon}\boldsymbol{\varepsilon}^{i-1} \left(\frac{dD}{d\boldsymbol{\varepsilon}} \right)^{i-1} \mathbf{B}_\varepsilon \Delta \mathbf{v} \right] dA \\ & + \int_A \mathbf{B}_\eta^T \left[(1-D^{i-1})\mathbf{C}_{\sigma\eta}\mathbf{B}_\eta \Delta \mathbf{v} - \mathbf{C}_{\sigma\eta}\boldsymbol{\eta}^{i-1} \left(\frac{dD}{d\boldsymbol{\varepsilon}} \right)^{i-1} \mathbf{B}_\eta \Delta \mathbf{v} \right] dA \\ & + \int_A \mathbf{B}_\eta^T \left[(1-D^{i-1})\mathbf{C}_{\mu\varepsilon}\mathbf{B}_\varepsilon \Delta \mathbf{v} - \mathbf{C}_{\mu\varepsilon}\boldsymbol{\varepsilon}^{i-1} \left(\frac{dD}{d\boldsymbol{\varepsilon}} \right)^{i-1} \mathbf{B}_\varepsilon \Delta \mathbf{v} \right] dA \\ & + \int_A \mathbf{B}_\eta^T \left[(1-D^{i-1})\mathbf{C}_{\mu\eta}\mathbf{B}_\eta \Delta \mathbf{v} - \mathbf{C}_{\mu\eta}\boldsymbol{\eta}^{i-1} \left(\frac{dD}{d\boldsymbol{\varepsilon}} \right)^{i-1} \mathbf{B}_\eta \Delta \mathbf{v} \right] dA \\ & = \int_s (\mathbf{N}^T \mathbf{t} + \text{grad } \mathbf{N}^T \mathbf{T}) ds - \int_A (\mathbf{B}_\varepsilon^T \boldsymbol{\sigma}^{i-1} + \mathbf{B}_\eta^T \boldsymbol{\mu}^{i-1}) dA. \end{aligned} \quad (28)$$

After some regrouping of the terms in the above relation, the finite element equation can be written as

$$(\mathbf{K}_{\varepsilon\varepsilon} + \mathbf{K}_{\varepsilon\eta} + \mathbf{K}_{\eta\varepsilon} + \mathbf{K}_{\eta\eta}) \Delta \mathbf{v} = \mathbf{F}_e - \mathbf{F}_i, \quad (29)$$

where the particular element stiffness matrices are defined as

$$\begin{aligned} \mathbf{K}_{\varepsilon\varepsilon} & = \int_A \mathbf{B}_\varepsilon^T \left[(1-D^{i-1})\mathbf{C}_{\sigma\varepsilon} - \mathbf{C}_{\sigma\varepsilon}\boldsymbol{\varepsilon}^{i-1} \left(\frac{dD}{d\boldsymbol{\varepsilon}} \right)^{i-1} \right. \\ & \quad \left. - \mathbf{C}_{\sigma\eta}\boldsymbol{\eta}^{i-1} \left(\frac{dD}{d\boldsymbol{\varepsilon}} \right)^{i-1} \right] \mathbf{B}_\varepsilon dA, \\ \mathbf{K}_{\varepsilon\eta} & = \int_A \mathbf{B}_\varepsilon^T (1-D^{i-1}) \mathbf{C}_{\sigma\eta} \mathbf{B}_\eta dA, \\ \mathbf{K}_{\eta\varepsilon} & = \int_A \mathbf{B}_\eta^T \left[(1-D^{i-1})\mathbf{C}_{\mu\varepsilon} - \mathbf{C}_{\mu\varepsilon}\boldsymbol{\varepsilon}^{i-1} \left(\frac{dD}{d\boldsymbol{\varepsilon}} \right)^{i-1} \right. \\ & \quad \left. - \mathbf{C}_{\mu\eta}\boldsymbol{\eta}^{i-1} \left(\frac{dD}{d\boldsymbol{\varepsilon}} \right)^{i-1} \right] \mathbf{B}_\varepsilon dA, \\ \mathbf{K}_{\eta\eta} & = \int_A \mathbf{B}_\eta^T (1-D^{i-1}) \mathbf{C}_{\mu\eta} \mathbf{B}_\eta dA. \end{aligned} \quad (30)$$

3.3. Calculation of constitutive stiffness matrices

For the analysis of the softening behavior of an arbitrary heterogeneous material all constitutive stiffness matrices appearing in Eq. (30) have to be known, which is not the case with the homogeneous material, as described later in the text. To compute these matrices, the second-order computational homogenization procedure is utilized, for which the basic relations are listed in Table 2. Generally, the procedure is performed in the multiscale analyses, where the quantities from lower scales have to be homogenized to put them in use at higher scales. The sequential micro-macro algorithm, which consists of the solutions of the boundary value problems at two different levels, is employed. The macrolevel refers to the model discretized by the aforementioned C^1 triangular finite elements, where in each integration point the microstructural contribution is included through the analysis of the RVE, in this paper discretized by the C^0 quadrilateral finite elements. In the table, the presented quantities denoted by the subscript ‘‘M’’ correspond to the macrolevel, while the subscript ‘‘m’’ indicates a microlevel quantity. In Eq. (31), \mathbf{x} is the spatial coordinate on the RVE boundary, while \mathbf{r} represents the microstructural fluctuation field. By means of the Hill-Mandel condition given by Eq. (32), the first- and second-order stress tensors can be derived in the form of Eq. (33), where \mathbf{D} and \mathbf{H} are the coordinate matrices which include all boundary nodes $i=1, 2, \dots, n$ of the RVE, while \mathbf{f}_b represents the RVE boundary nodal force vector. Taking into account the internal (subscript ‘‘a’’) and the boundary (subscript ‘‘b’’) contributions of the RVE, the finite element equation for the nonlinear problems can be written in the incremental form as presented in Eq. (35). Employing Eq. (20), the incremental form of the first- and second-order stress tensors represented by Eq. (38) can then easily be obtained, which yields the tangent stiffness matrices given by Eq. (39). Detailed information about the second-order homogenization procedure can be found in (Kaczmarczyk et al., 2008) and (Lesičar et al., 2014).

In the case of material homogeneity, material isotropy, and symmetry of the RVE considered the tangent stiffness matrices $\mathbf{C}_{\sigma\eta}$ and $\mathbf{C}_{\mu\varepsilon}$ are equal to zero (Kaczmarczyk et al., 2008). The remaining two tangent stiffness matrices can be computed analytically (Kouznetsova et al., 2004; Kaczmarczyk et al., 2008), which may

Table 2.
Basic relations of the second-order homogenization.

The RVE displacement field:

$$\mathbf{u}_m = \mathbf{x}^T \boldsymbol{\varepsilon}_M + \frac{1}{2} \mathbf{x}^T \boldsymbol{\eta}_M \mathbf{x} + \mathbf{r}. \quad (31)$$

The Hill-Mandel condition:

$$\frac{1}{V} \int_V (\delta \boldsymbol{\varepsilon}_m^T \boldsymbol{\sigma}_m) dV = \delta \boldsymbol{\varepsilon}_M^T \boldsymbol{\sigma}_M + \delta \boldsymbol{\eta}_M^T \boldsymbol{\mu}_M. \quad (32)$$

The first- and second-order stress tensors:

$$\begin{aligned} \boldsymbol{\sigma}_M &= \frac{1}{V} \mathbf{D} \mathbf{f}_b, \\ \boldsymbol{\mu}_M &= \frac{1}{V} \mathbf{H} \mathbf{f}_b, \end{aligned} \quad (33)$$

where

$$\begin{aligned} \mathbf{D} &= \frac{1}{2} \begin{bmatrix} \mathbf{D}_1^T & \mathbf{D}_2^T & \dots & \mathbf{D}_n^T \end{bmatrix}, \\ \mathbf{H} &= \frac{1}{2} \begin{bmatrix} \mathbf{H}_1^T & \mathbf{H}_2^T & \dots & \mathbf{H}_n^T \end{bmatrix}, \end{aligned} \quad (34)$$

and

$$\begin{aligned} \mathbf{D}_i &= \frac{1}{2} \begin{bmatrix} 2x & 0 & y \\ 0 & 2y & x \end{bmatrix}, \\ \mathbf{H}_i &= \frac{1}{2} \begin{bmatrix} 2x^2 & 0 & 2y^2 & 0 & xy & 0 \\ 0 & 2y^2 & 0 & 2x^2 & 0 & xy \end{bmatrix}. \end{aligned}$$

The partitioned finite element equation in incremental form:

$$\begin{bmatrix} K_{aa} & K_{ab} \\ K_{ba} & K_{bb} \end{bmatrix} \begin{bmatrix} \Delta \mathbf{u}_a \\ \Delta \mathbf{u}_b \end{bmatrix} = \begin{bmatrix} \Delta \mathbf{f}_a \\ \Delta \mathbf{f}_b \end{bmatrix}. \quad (35)$$

In the convergence state

$$\begin{aligned} \Delta \mathbf{f}_a &= \mathbf{0}, \\ \Delta \mathbf{f}_b &= \tilde{K}_{bb} \Delta \mathbf{u}_b, \end{aligned} \quad (36)$$

with $\tilde{K}_{bb} = K_{bb} - K_{ba} K_{aa}^{-1} K_{ab}$.

The RVE boundary nodes displacement increment:

$$\Delta \mathbf{u}_b = \mathbf{D}^T \Delta \boldsymbol{\varepsilon}_M + \mathbf{H}^T \Delta \boldsymbol{\eta}_M. \quad (37)$$

The incremental values of the first- and second-order stress tensors:

$$\begin{aligned} \Delta \boldsymbol{\sigma}_M &= \frac{1}{V} (\mathbf{D} \tilde{K}_{bb} \mathbf{D}^T \Delta \boldsymbol{\varepsilon}_M + \mathbf{D} \tilde{K}_{bb} \mathbf{H}^T \Delta \boldsymbol{\eta}_M), \\ \Delta \boldsymbol{\mu}_M &= \frac{1}{V} (\mathbf{H} \tilde{K}_{bb} \mathbf{D}^T \Delta \boldsymbol{\varepsilon}_M + \mathbf{H} \tilde{K}_{bb} \mathbf{H}^T \Delta \boldsymbol{\eta}_M). \end{aligned} \quad (38)$$

The tangent stiffness matrices:

$$\begin{aligned} \mathbf{C}_{\sigma\varepsilon} &= \frac{1}{V} \mathbf{D} \tilde{K}_{bb} \mathbf{D}^T, \\ \mathbf{C}_{\sigma\eta} &= \frac{1}{V} \mathbf{D} \tilde{K}_{bb} \mathbf{H}^T, \\ \mathbf{C}_{\mu\varepsilon} &= \frac{1}{V} \mathbf{H} \tilde{K}_{bb} \mathbf{D}^T, \\ \mathbf{C}_{\mu\eta} &= \frac{1}{V} \mathbf{H} \tilde{K}_{bb} \mathbf{H}^T. \end{aligned} \quad (39)$$

be written symbolically in the form

$$\begin{aligned} \mathbf{C}_{\sigma\varepsilon} &= \mathbf{C}_{\sigma\varepsilon}(E, \nu), \\ \mathbf{C}_{\mu\eta} &= \mathbf{C}_{\mu\eta}(E, \nu, l), \end{aligned} \quad (40)$$

where l denotes the microstructural length scale. On the other hand, the stiffness matrices can be also computed numeri-

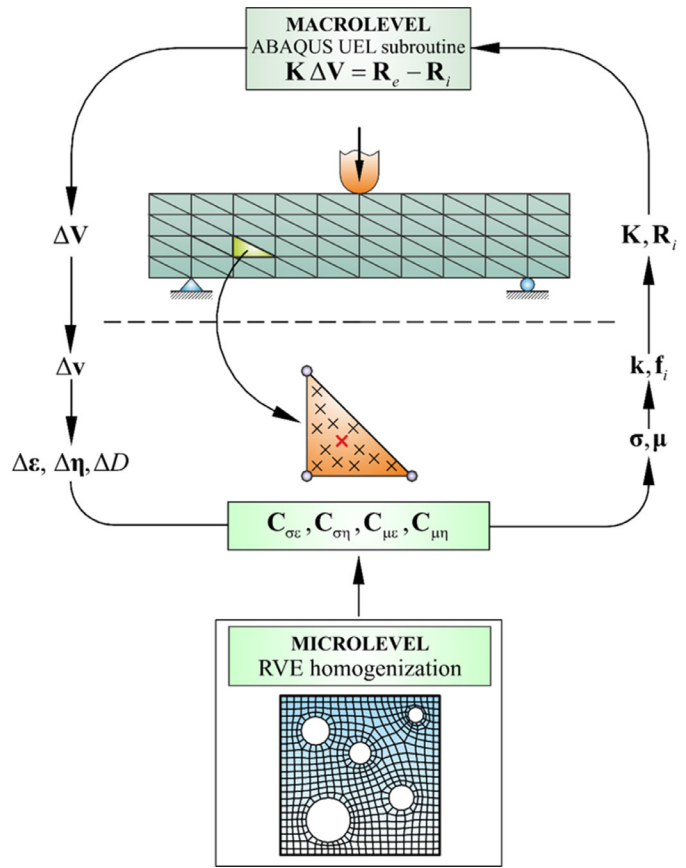


Fig. 2. Scheme of the damage algorithm.

cally using the homogenization procedure as already done in (Lesičar et al., 2014). Therein the microstructural parameter is expressed by the relation

$$l^2 = \frac{L^2}{12}, \quad (41)$$

where L is the RVE side length. As displayed above, the material nonlocality is included into the second-gradient continuum theory through the higher-order constitutive matrices $\mathbf{C}_{\sigma\eta}, \mathbf{C}_{\mu\varepsilon}$ and $\mathbf{C}_{\mu\eta}$ in terms of the microstructural parameter l . When these matrices are multiplied by the term $(1 - D)$ according to Eq. (22), the nonlocality decreases if the damage rises.

3.4. Analysis procedure

The analysis procedure is concisely shown as a flowchart in Fig. 2. It should be noted that this is not a true multiscale algorithm which includes subsequent solving of the two boundary value problems, the one at the macrolevel and the other at the microlevel. Instead, the boundary value problem has to be solved here only for the macromodel, while the microstructural RVE analysis, comprised only of the stiffness homogenization, is performed in a preprocessing step to obtain the values of the constitutive stiffness tensors. Since the linear elastic material behavior is considered in the presented damage analysis, the homogenized solutions do not depend on the macroscale deformation. Therefore, the homogenization procedure has to be performed only once in each analysis. The homogenized stiffness values then enter the constitutive relations, and remain constant until the end of the nonlinear damage analysis. When the damage is initiated in the model, the elastic stiffness is being reduced according to (1) and to the damage enhanced constitutive relations (22) as well. In each

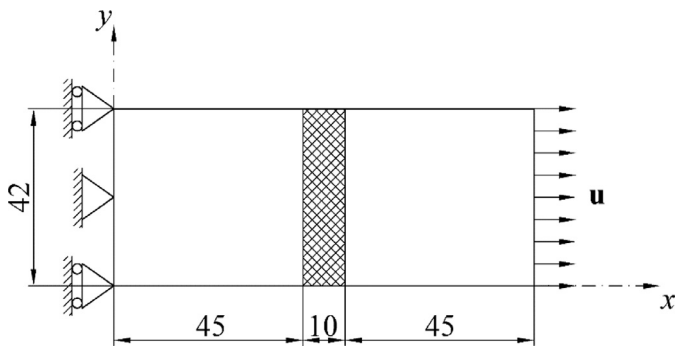


Fig. 3. Geometry and boundary conditions of the plate subjected to tensile load.

finite element integration point, the incremental-iterative procedure is carried out, where the stress and double stress tensors are calculated from the updated values of the strain tensor, the second-order strain tensor and the damage variable, as well as the constant elastic stiffness tensors obtained in the preprocessing step. The presented damage algorithm together with the formulation of the triangular finite element is implemented into the FE program ABAQUS employing the user subroutines.

4. Numerical examples

4.1. Plate with an imperfect zone subjected to tensile load

4.1.1. Homogeneous plate, algorithm verification and damage responses

The presented algorithm is verified in a benchmark problem already studied in (Yang and Misra, 2010), where only a homogeneous material is considered. In this contribution the analysis is extended to the consideration of heterogeneous materials, too. The geometry and boundary conditions of the rectangular plate with an imperfect zone under tension are shown in Fig. 3. The Mazars equivalent strain measure (3) is used together with the damage evolution governed by the linear softening. The material data are: the Young's modulus $E=20,000$ N/mm², the Poisson's ratio $\nu=0.25$, the limit elastic strain $\kappa_0=0.0001$, the equivalent strain corresponding to the fully damaged state $\kappa_u=0.0125$. The horizontal displacement of $u=0.0325$ mm is prescribed at the right edge. In order to trigger localization, the Young's modulus is reduced by 10% in the 10 mm wide zone in the middle hatched area of the plate. Along the vertical edges the second-order derivatives of the displacement component in the normal direction, $u_{1,11}$ and $u_{1,22}$, together with the mixed derivatives, $u_{1,12}$ and $u_{2,12}$, are suppressed. The first-order derivatives associated with the shear deformation, $u_{1,2}$ and $u_{2,1}$, are also set to zero. These boundary conditions yield the straight vertical edges. Here, the indices 1 and 2 refer to the Cartesian coordinates x and y , respectively.

The solutions of the same numerical example are obtained by means of the EFG meshless method in Yang and Misra (2010). Therein, the constitutive tensors are derived for the materials with granular microstructure, so the underlying microstructural theory differs when compared with the second-order homogenization approach. The constitutive model is restricted only to homogeneous materials, where the corresponding stiffness tensors can be written in the form of Eq. (40) with the particle radius r instead of the microstructural parameter l . The same constitutive model is used for the computation of the softening response of the plate by means of the proposed FEM algorithm. The damage responses obtained for the same microstructural values and using different approaches are presented in Fig. 4. In this numerical example, the distributions of the damage and equivalent strain are considered along the

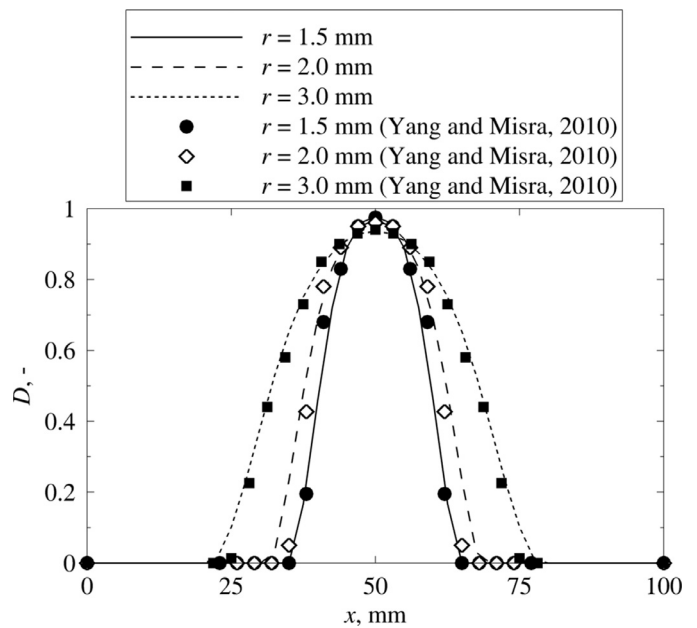


Fig. 4. Comparison of damage profiles along the horizontal central axis of the plate obtained using the presented FEM damage model to the EFG results from the literature.

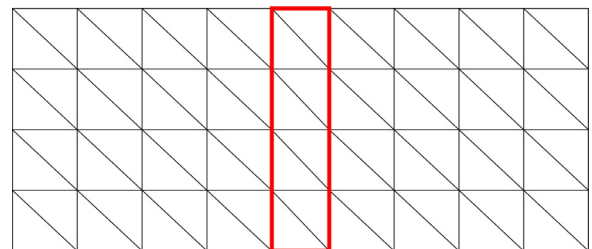


Fig. 5. The coarsest finite element mesh of the plate under tension.

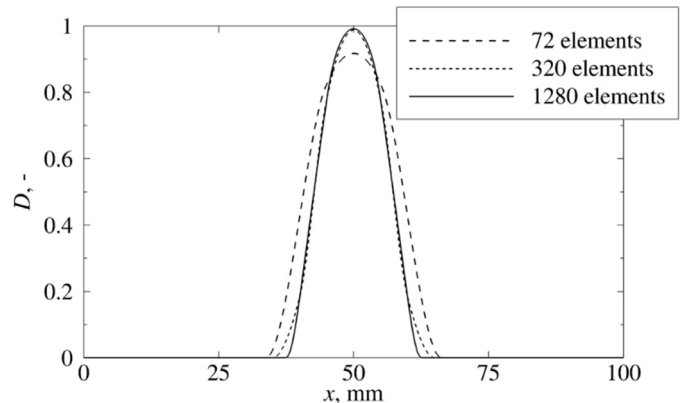


Fig. 6. Comparison of damage profiles along horizontal central axis of the plate under tension for three different mesh densities.

horizontal central axis of the plate, crossing the hinged joint at $y=21$ mm.

As can be seen from Fig. 4, the calculated damage profiles show very good agreement with the solutions from the literature. The figure also illustrates the effect of the microstructural size on the macrostructural behavior. The increase in the microstructural values leads to the expansion of the localization zone and a slight decrease in the peak damage values, as expected.

Furthermore, the mesh sensitivity of the proposed algorithm is examined by using the three different finite element discretizations. Fig. 5 presents the coarsest mesh of 72 elements with the

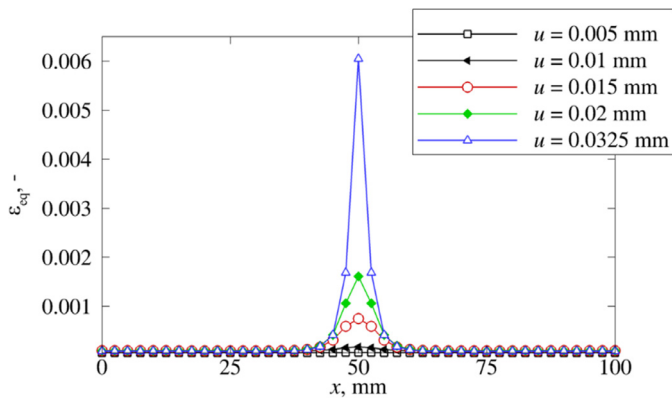


Fig. 7. Evolution of the equivalent elastic strain ε_{eq} along horizontal central axis of the plate for different loading levels.

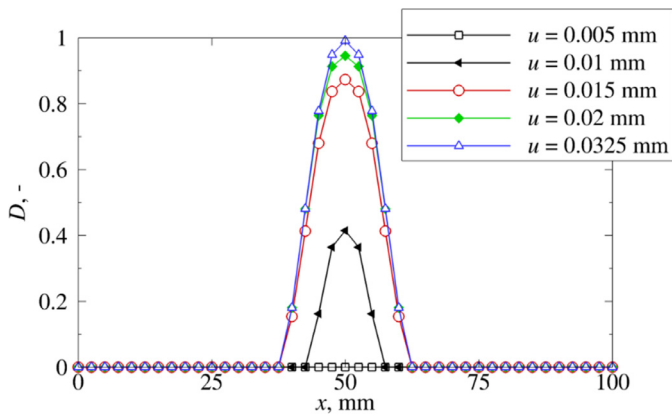


Fig. 8. Evolution of the damage variable D along horizontal central axis of the plate for different loading levels.

reduced material properties in the marked area covered by only few elements. A homogeneous material with the internal length scale of $l = 1.5$ mm is considered.

As evident from Fig. 6, the reduction of the element size in the last two discretizations does not lead to the further localization of the damage profile in the softening zone, which proves that the presented damage model is independent on the mesh refinement. It is also interesting to note that values of the nodal variables computed by the coarsest and the finest discretization are quite similar, leading to the conclusion that convergence can be achieved with a relatively coarse mesh and accordingly with a significant reduction of the computational time.

Next, the evolution of the equivalent elastic strain measure as well as the damage variable is depicted in Figs. 7 and 8. It can be noted that the growth of the equivalent elastic strain emerges within the imperfection and rather early in the softening process reaches its final width, which does not change in the subsequent loading stages. Instead, the localization drastically intensifies during final loading stages in the narrow region in the middle of the plate, which is basically a continuum representation of a macroscopic crack. In Geers et al. (1998) the similar problem is studied in only one dimension employing the conventional implicit gradient enhancement, resulting in an unacceptable growth of the damage zone. Instead of the localization into a macroscopic crack, the expansion of the damaged zone with the loading progression is reported for the analyzed bar in tension. The solutions obtained by the strain gradient formulation proposed in this contribution show no such spurious damage growth, which is obviously an advantage when compared with the conventional implicit gradient formulation. The described physically meaningless phenomenon is eliminated in Geers et al. (1998) in the form of the somewhat compli-

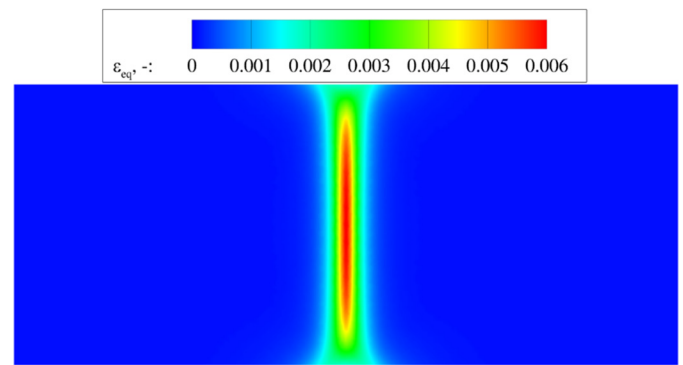


Fig. 9. Distribution of the equivalent elastic strain ε_{eq} for homogeneous material at failure stage.

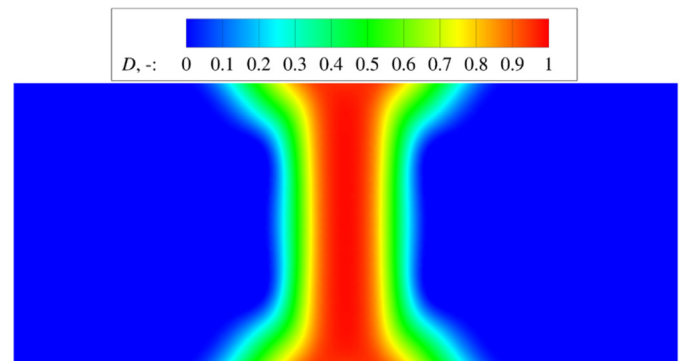


Fig. 10. Distribution of the damage D for homogeneous material at failure stage.

cated strain-based transient-gradient damage method which couples the nonlocal effect to the local deformation state of the material. It can be noted that a similar thing is basically done in the present contribution, where the local and nonlocal effects are coupled through the damage constitutive relations of the second-gradient continuum theory, knowing that the damage variable is a function of the local equivalent strain measure.

For a better perception of the softening process in the failure deformation stage, the distributions of equivalent elastic strain measure and damage variable are displayed in Fig. 9 and Fig. 10, respectively. In Fig. 9 the localized deformation band can be clearly seen, with the highest values of equivalent elastic strain in the central part of the plate, being a consequence of the lateral contraction. Namely, since the edges defined by the normal vectors in vertical direction are free boundaries, the material is more pliable in their vicinity and it stretches in the loading direction more than the material in the central part of the plate. Besides, due to the Poisson's effect, it contracts more laterally and therefore does not contribute to the Mazars equivalent elastic strain measure defined in Eq. (3). As evident, the damage distribution in Fig. 10 appears overly spread in contrast to the equivalent elastic strain distribution in Fig. 9. This phenomenon can be explained by considering the damage irreversibility and knowing that the fracture usually starts as a zone of high material nonlocal behavior, and ends as a narrow localized deformation band where nonlocality is significantly reduced. Additionally, it is worth to mention that softening laws for the quasi-brittle materials usually give rather high damage values for the equivalent elastic strain values just slightly above the limit strain κ_0 .

The equivalent stress field defined by

$$\sigma_{eq} = (1 - D)E\varepsilon_{eq} \quad (42)$$

is depicted in Fig. 11, where its reduction can clearly be seen in the area which coincides with the localization zone shown in Fig. 9.

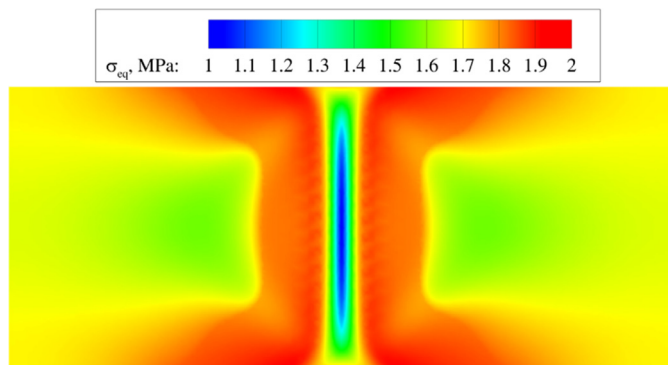


Fig. 11. Distribution of the equivalent stress σ_{eq} for homogeneous material at failure stage.

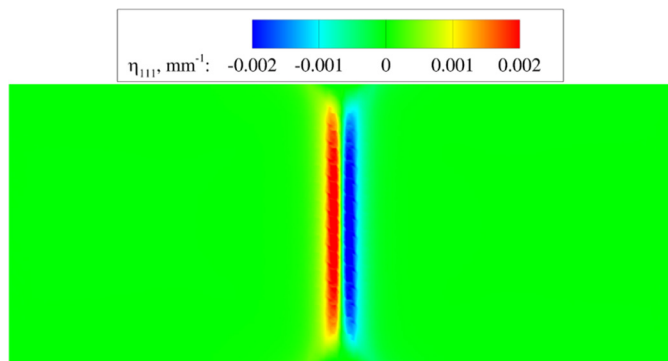


Fig. 12. Distribution of the strain gradient component η_{111} for homogeneous material at failure stage.

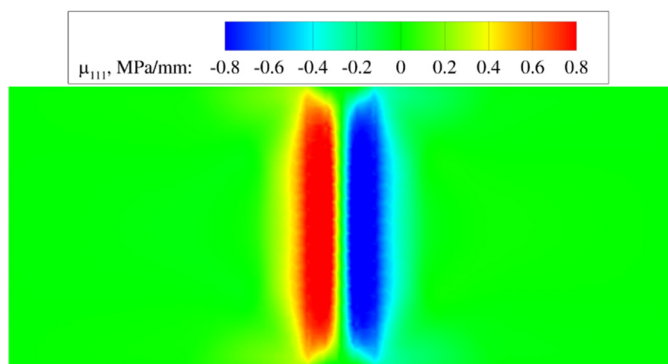


Fig. 13. Distribution of the double stress component μ_{111} for homogeneous material at failure stage.

As it is obvious from Fig. 9, the softening of the material is at its highest in the middle of the plate, whereas its intensity decreases towards the free boundaries. Therefore, it is to expect that the material at the free horizontal boundaries carries more load than that which is closer to the central part of the plate. The direct consequence of such a behavior are the higher equivalent stress values of the material closer to the boundaries, taking into account the Eq. (42). Of course, with the increasing distance from the highly damaged area, where the high gradients are present, the stress field becomes more uniform towards the left and the right vertical boundaries, where the straight edges are enforced.

The contour plots of the strain gradient component η_{111} and the corresponding double stress component μ_{111} are shown in Figs. 12 and 13, respectively. As evident from Fig. 12, the two symmetrically mirrored strain gradient bands are formed on the edges of the localization band displayed in Fig. 9. In the narrow area in the mid-

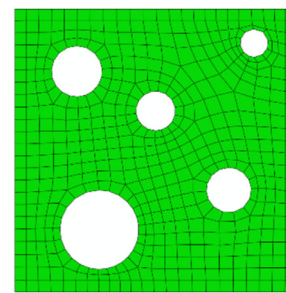


Fig. 14. RVE_0 described by the size $L = 5.2$ mm ($l = 1.5$ mm), average hole radius $r_{ave} = 1.118$ mm and porosity $e = 0.13$.

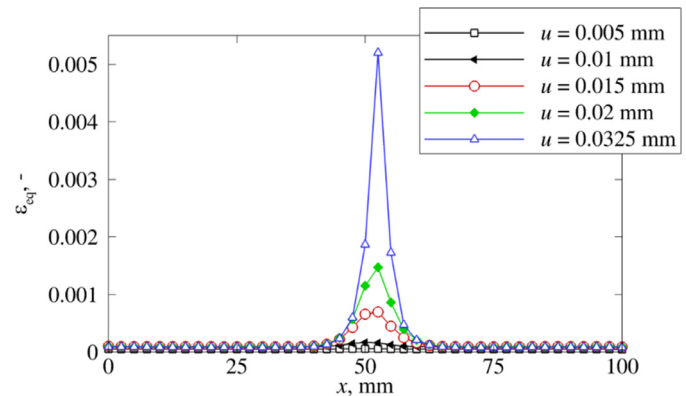


Fig. 15. Evolution of the equivalent elastic strain ϵ_{eq} along horizontal central axis of the heterogeneous plate for different loading levels.

dle of the localization band, where the strain ϵ_{11} reaches its peak value, the strain gradient component η_{111} changes the sign and it is equal or very close to zero. The double stress component μ_{111} in Fig. 13 closely resembles the strain gradient component η_{111} , which is logical due to their direct connection through the second constitutive relation of the strain gradient continuum theory shown in Eq. (22).

4.1.2. Damage responses of heterogeneous plate

The next step is the consideration of damage responses of the heterogeneous plate. The materials used in the following calculations are described by the porous RVEs at microstructural level. Here all homogenized stiffness tensors according to the damage enhanced constitutive relations (22) are included in the computation. As stated earlier in the paper, the influence of the heterogeneous microstructure described by the RVE on the macrostructural anisotropic response is carried by the non-diagonal constitutive tensors of the fifth order, $C_{\sigma\eta}$ and $C_{\mu\epsilon}$. The homogenization process has been described in the previous sections. The RVEs differ in the size, porosity and in the number, size and distribution of the holes. The material properties are the same as for the homogeneous plate. Firstly, a simple RVE, presented in Fig. 14, is used to analyze the plate softening behavior. This RVE geometry is labelled as RVE_0 in the following consideration.

The evolution of the equivalent elastic strain measure and the damage variable is depicted in Figs. 15 and 16 for different loading levels. The distributions of the same variables over the whole plate at the failure stage are depicted as contour plots in Figs. 17 and 18, respectively. A slight shift of the presented variables to the right can be seen from the given diagrams and contour plots when compared with the diagrams and contour plots concerning the homogeneous material, given in Figs. 7–10. Such behavior can be ascribed to the microscopic heterogeneity which is mathematically expressed by the relatively high values of the non-diagonal $C_{\sigma\eta}$

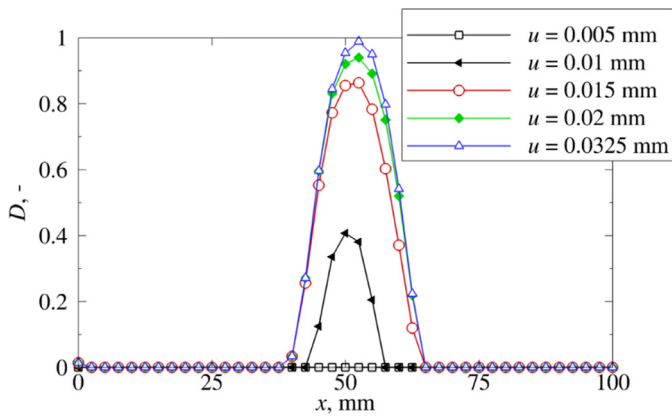


Fig. 16. Evolution of the damage variable D along horizontal central axis of the heterogeneous plate for different loading levels.

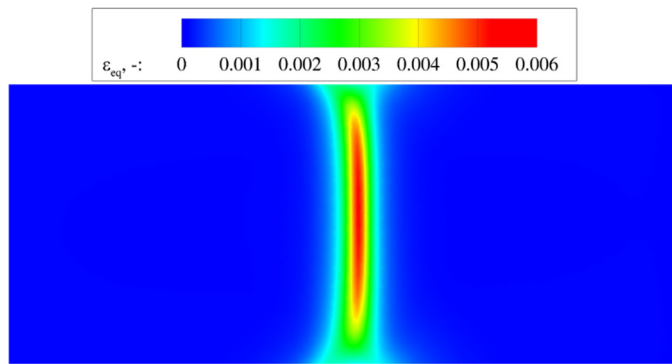


Fig. 17. Distribution of the equivalent elastic strain ε_{eq} for heterogeneous material represented by RVE_0 at failure stage.

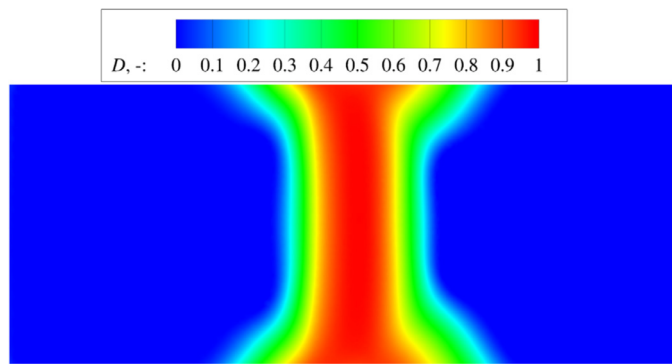


Fig. 18. Distribution of the damage D for heterogeneous material represented by RVE_0 at failure stage.

and $C_{\mu\varepsilon}$ matrices in the damage enhanced constitutive Eq. (22). As obvious, the differences between the damage distributions in Figs. 10 and 18 are just barely visible, but in order to retain the consistence of the whole work presented, the latter figure is shown too.

Additionally, if the softening analysis is performed by the constitutive tensors acquired for the RVE_0 rotated for 180°, the obtained results are symmetrically mirrored to the ones depicted in Figs. 15–18, as expected. Taking this into account, and knowing that microscopic samples in the form of RVE_0 are randomly distributed in various directions in the real material, an average contribution of all RVEs could lead to the isotropic macrostructural response. Thus, it is clear that the given academic RVE lacks the statistical representativeness, i.e. it is not representative in a global sense, for the whole material. From comparison of Fig. 7 and Fig. 15, it can be noted that the maximum equivalent strain value

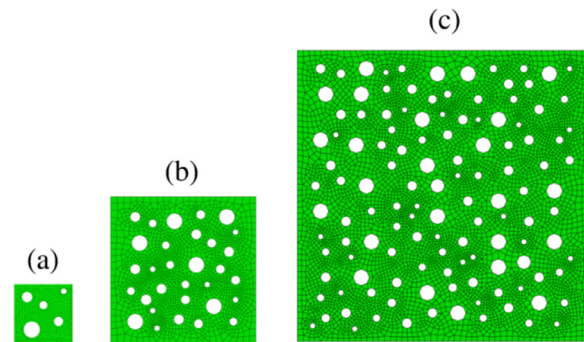


Fig. 19. Three different-sized samples of the same heterogeneous material: (a) RVE_1 with the size $L = 3$ mm ($l = 0.87$ mm), (b) RVE_2 with the size $L = 7.5$ mm ($l = 2.16$ mm) and (c) RVE_3 with the size $L = 15$ mm ($l = 4.33$ mm).

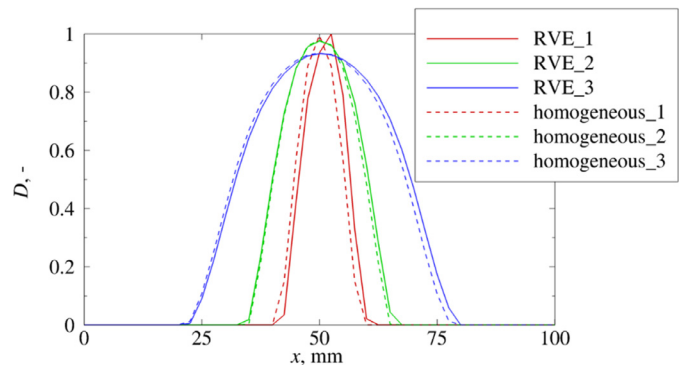


Fig. 20. Comparison of damage profiles along horizontal central axis of the plate for heterogeneous material represented by three different-sized RVEs and homogeneous material of the corresponding internal length scales.

for the homogenous material is slightly higher than that for the heterogeneous material. Because the heterogeneous plate is more pliable in the whole domain due to the holes in the microstructure, the bulk material outside of the localization zone permits higher equivalent strain in this particular area, leading to the slightly smaller equivalent strain in the middle of the plate when compared with the equivalent strain in the homogenous plate.

As for the homogenous material, the increase in the RVE size, which expresses the change in the microstructural interactions, leads to the expansion of the localization zone. Here the three different-sized RVEs of the same heterogeneity are considered, which is defined by the porosity of $e = 0.13$ and the average hole radius of $r_{ave} = 0.744$ mm, as shown in Fig. 19. In Fig. 20, the damage profiles for the three described heterogeneous RVEs are compared to the damage responses of the homogeneous material with the same nonlocal parameter l .

As can be seen from Fig. 20, a slight deviation from the damage profile of the corresponding homogenous material is shown for the damage profile obtained using the smallest RVE, while this difference is much less pronounced for the other two heterogeneous samples. This confirms that for statistically well-defined RVE, the damage distribution in qualitative sense should not deviate significantly from the damage distribution for the homogenous material of the same internal length scale. Next, an analysis employing the two different heterogeneous materials, defined by the RVEs of the same side length of $L = 6.9$ mm and porosity of $e = 0.13$, but different average hole radii, $r_{ave} = 1.5$ and 0.6 mm, is performed. Their damage responses are compared to the damage response of the homogeneous material defined by the same RVE size, as shown in Fig. 21. As expected, the damage response of the heterogeneous material with larger average hole radius shows a notable shift when compared to the damage response of the corresponding

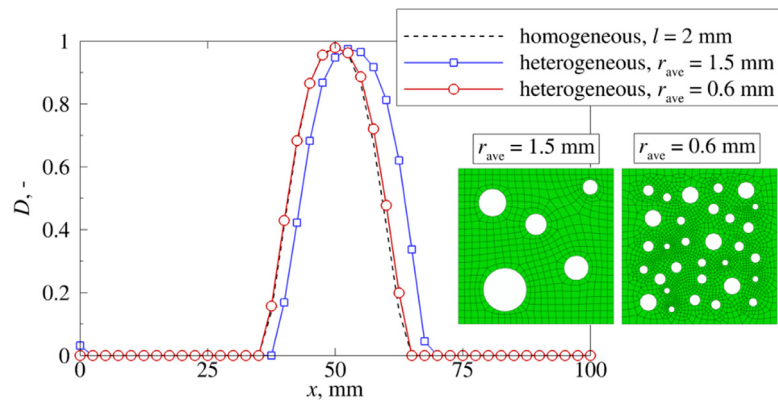


Fig. 21. Comparison of damage profiles along horizontal central axis of the plate for two heterogeneous materials of the same porosity and corresponding homogeneous material.

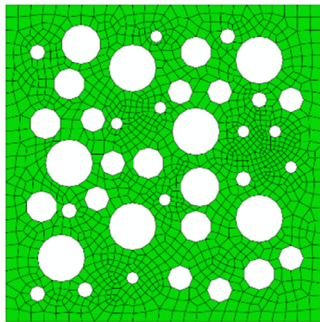


Fig. 22. RVE_4 described by the size $L = 1.73$ mm ($l = 0.5$ mm), average hole radius $r_{ave} = 0.075$ mm and porosity $e = 0.27$.

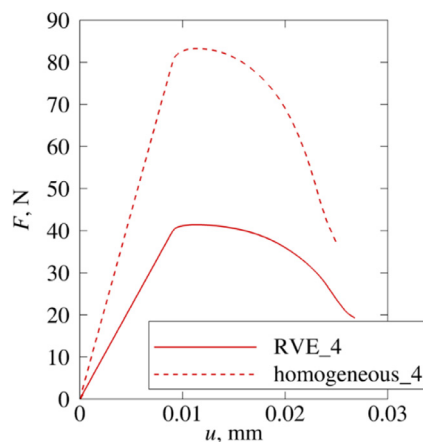


Fig. 23. Comparison of structural responses of the plate under tension for heterogeneous material represented by RVE_4 and homogeneous material of the same internal length scale.

homogeneous material. Obviously, this difference is much smaller for the heterogeneous material with smaller average hole radius. The aforementioned shift in the case of the heterogeneous material defined by the $r_{ave} = 1.5$ mm occurs as a consequence of the larger macrostructural anisotropic response.

Finally, the RVE with the higher porosity e , labelled RVE_4 and depicted in Fig. 22, is employed for the calculation of the stiffness matrices required for the softening analysis.

Because of the higher RVE porosity, a significant decrease in the loading associated with the start of the softening process is expected, which is shown in the load-displacement diagram displayed in Fig. 23. In the diagram, the reaction forces at the right

end of the plate are plotted versus the imposed displacement for both the heterogeneous material defined by the RVE_4 and the corresponding homogeneous material. It can clearly be seen that reduced stiffness of the heterogeneous material causes the softening initiation at much lower load level than in the case of the homogeneous material.

It is to note that the presented damage analysis of the heterogeneous structure is based on the microlevel homogenization procedure in order to compute the stiffness matrices, while the softening response is modeled by the damage enhanced constitutive relations (22) at the macrolevel. Although the proposed analysis has its advantages due to the simplicity and low computational costs, it should be stressed that a true multiscale analysis should be performed to obtain more accurate results. Namely, a more accurate computation of the damage response of heterogeneous materials requires the application of the constitutive relations directly at the microlevel considering all material constituents in the RVE and, after a homogenization procedure, transfer of the state variables to the macrostructural level. The derivation of this multiscale approach is out of the scope of this contribution and will be considered in the authors' further research.

4.2. Shear band problem

The second example, where further capacities of the presented algorithm are shown, is a plate with an imperfect zone subjected to compressive load, presented in Fig. 24a. Due to symmetry, only the upper half of the plate is discretized by the C^1 continuity triangular finite element employing appropriate boundary conditions, as depicted in Fig. 24b. The compressive loading is applied using a direct displacement control, where the analysis stops at the vertical displacement of $v = 0.08$ mm. Firstly the homogeneous material is considered which is characterised by the Young's modulus $E = 20,000$ N/mm² and the Poisson's ratio $\nu = 0.2$. For modeling of damage responses, a modified von Mises equivalent elastic strain measure (5) together with the exponential softening law (7) is used, for which the parameters are set to: $\kappa_0 = 0.0001$, $\alpha = 0.99$ and $\beta = 300$. To induce localization, the reduced value of $\kappa_0 = 0.00005$ as a material imperfection is imposed on the small region of $h/10 \times h/10$ as shown in Fig. 24a. The material microstructural parameter is taken as $l = 2$ mm. Since both the symmetry plane and the loaded edge have to remain straight during the analysis, the boundary conditions for the straight edge are enforced there. Herein, the second-order derivatives of the displacement component in the normal direction, $u_{2,11}$ and $u_{2,22}$, together with the mixed derivatives, $u_{1,12}$ and $u_{2,12}$, are suppressed. The first-order derivatives associated with the shear deformation, $u_{1,2}$ and $u_{2,1}$, are

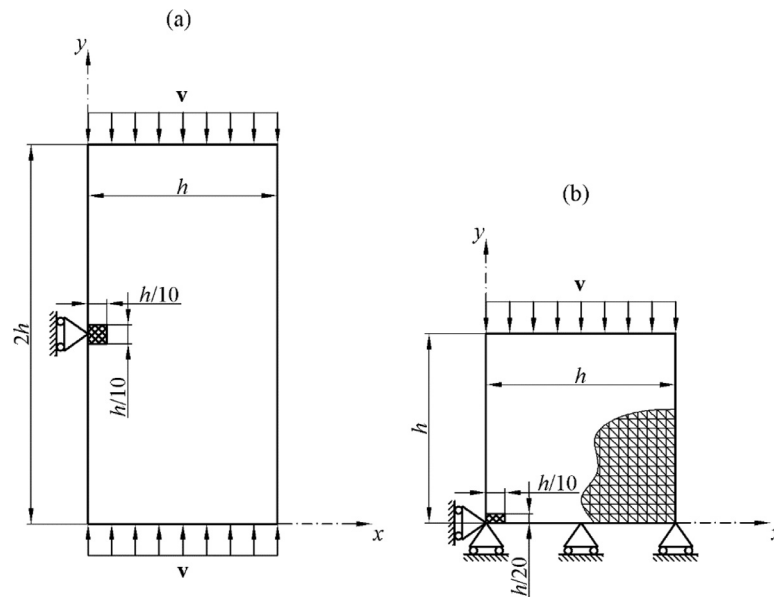


Fig. 24. (a) Geometry and boundary conditions of the plate with an imperfect zone subjected to compressive load and (b) computational model consisting of upper half of the plate and appropriate boundary conditions, with a depicted mesh detail.

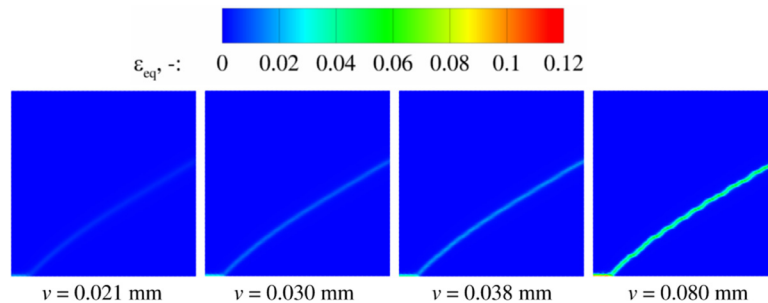


Fig. 25. Distribution of the equivalent elastic strain ε_{eq} through several loading stages for homogeneous material.

also set to zero. As mentioned before, the indices 1 and 2 refer to the Cartesian coordinates x and y , respectively.

The same specimen has already been studied by Simone et al. (2004) with the adoption of the damage model based on the conventional implicit gradient enhancement, resulting in the spurious damage growth along the bottom horizontal boundary with the rise of the deformation level, which is obviously a non-physical behavior. As discussed in (Poh and Sun, 2017), the conventional nonlocal models, being either integral or gradient, deal with a material softening employing a constant interaction domain throughout the entire loading history. This leads to the transfer of the energy from the damage process zone to a neighboring elastically unloading region, resulting in the smeared damage distribution within and beyond the shear band. The consequence of such unwanted behavior is the inability of a macrocrack formation.

The regularizing capabilities of the proposed formulation in terms of the elimination of the spurious damage growth are shown by plotting the distribution of the equivalent elastic strain in Fig. 25 and the distribution of the damage in Fig. 26, through several loading stages. The results are compared with the solutions obtained in Simone et al. (2004). For a better comparison of the given variables, the loading levels chosen for the contour plots are the same as shown in Simone et al. (2004), where the aforementioned spurious damage growth is observed. It can clearly be seen, especially from Fig. 26, that in the present contribution the shear band starts to develop from the defect region and propagates to-

wards the right edge of the plate model, as expected. In the formulation in Simone et al. (2004) the shear band is developing along the horizontal boundary, which is unrealistic. Furthermore, the contour plots obtained in the present formulation display that once the shear band reaches its final width, which is very early in the softening process, the localization of the deformation continues in its center until the shear fracture occurs. This is particularly visible in Fig. 25 starting from the loading level at $v=0.021$ mm. At lower displacements, a development of the localized deformation cannot be seen because the equivalent elastic strain is just slightly beyond the critical value of κ_0 . This can be confirmed by the damage distribution images in Fig. 26 and knowing that even for a very small equivalent elastic deformation the damage field rises to very high values in the case of exponential softening law. A similar shear band evolution accompanied with the strong localization and no spurious damage growth is also obtained in (Poh and Sun, 2017), where the localizing gradient damage model derived in the micromorphic framework is used. The similar realistic results are observed in the experimental investigations in (Alshibli and Sture, 2000) as well.

To examine the mesh sensitivity, an additional finite element discretization of 800 triangular finite elements is considered, opposed to the 3200 elements used so far. Generally, the accurate results could also be obtained by using a non-uniform mesh and much smaller number of finite elements, as proven earlier in the paper. In this case, in order to maintain the mesh uniformity for simplicity, such fine discretization is conditioned by a very small

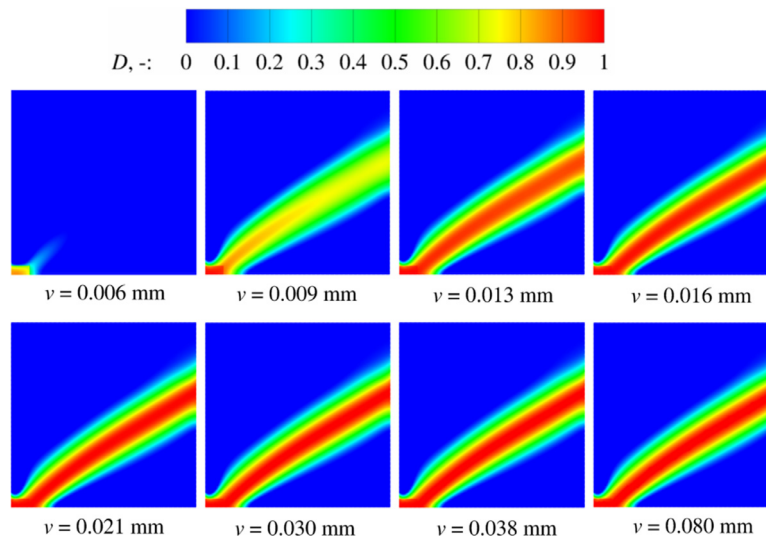


Fig. 26. Distribution of the damage D through several loading stages for homogeneous material.

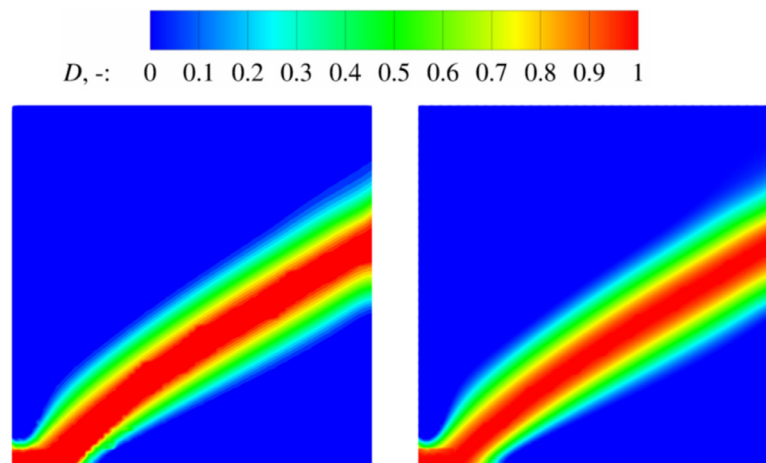


Fig. 27. Comparison of damage distribution D for homogeneous material for two different discretizations consisting of 800 (left) and 3200 (right) triangular finite elements.

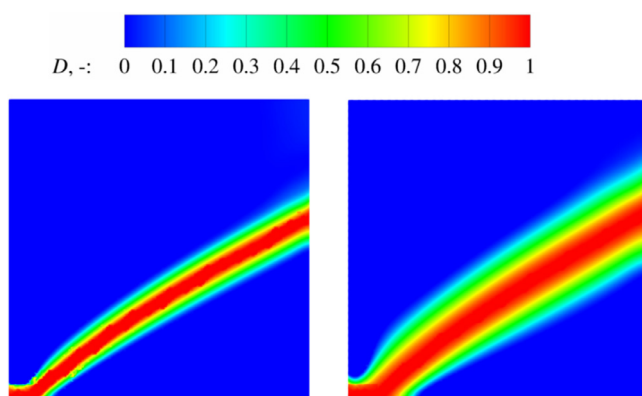


Fig. 28. Comparison of damage distribution D for homogeneous material defined with the internal length scales $l = 1$ mm (left) and $l = 2$ mm (right).

imperfect region. As portrayed in Fig. 27, there are no differences in the damage responses. The damage profile is correctly captured for the two different discretization sizes.

If a smaller internal length scale is used, the shear band decreases in the width, as expected, which is shown in Fig. 28.

Calculation of the damage response of the heterogeneous material in the context of the shear band problem is performed with an RVE qualitatively similar to the RVE_4 shown in Fig. 22, but defined with the side length of $L = 6.9$ mm and the average hole radius $r_{ave} = 0.297$ mm. Here, the whole plate model depicted in Fig. 24a has to be used due to the material anisotropy which is a consequence of the microstructural heterogeneity. The contour plots displaying the damage responses of the considered heterogeneous and homogeneous material show barely notable differences and are therefore not shown. On the other hand, from the load-displacement diagram depicted in Fig. 29, a very pronounced decrease in the reaction force at the initial softening can be seen for the heterogeneous material when compared to the reaction force of the corresponding homogeneous material, similar as in the previous numerical example.

Finally, it should be stressed that the presented damage model can successfully predict the strain localization, as well as the damage growth without any spurious phenomena in contrast to the formulation using the conventional implicit gradient-enhanced damage model yielding the non-physical damage response. It is believed that the main reason for this ability lies in the constitutive damage model based on the strain gradient theory, where the right-hand sides of both equations are influenced by the same factor $(1 - D)$ as a result of the damage growth. If this factor is

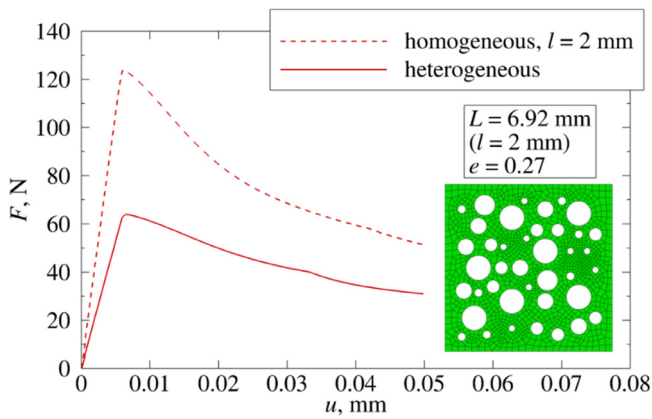


Fig. 29. Comparison of structural responses of the plate under compression for heterogeneous material and homogeneous material of the same internal length scale.

observed as a reduction mechanism of the higher-order stiffness tensors $C_{\sigma\eta}$, $C_{\mu\varepsilon}$ and especially $C_{\mu\eta}$, which are directly connected to the size of the microstructural interaction area, i.e. a nonlocal material behavior, it can be said that the intensity of the microstructural interactions decreases with the damage progression and that the material gradually loses the ability to behave non-locally at a particular damaged point. Such material behavior is physically completely valid and motivated by the fact that a fracturing of quasi-brittle materials usually starts as a diffuse network of microcracks, represented by a large microstructural interaction domain, and ends with their localization into a macrocrack, characterized by almost non-existent intensity of microstructural interactions, as discussed in more detail in (Poh and Sun, 2017).

5. Conclusion

A computational approach employing the strain gradient continuum theory for the modeling of quasi-brittle damage phenomena is proposed. The model is based on the isotropic damage law so that right-hand sides of the constitutive relations are pre-multiplied by the same term governing the damage process. The growth of the damage causes this term to decrease, which not only ensures the softening of the material by reducing the values of the constitutive tensors, but it also effects the size of the microstructural interaction domain, included in the constitutive tensors definition, in the same way. The latter is mandatory for the correct description of the final localized deformation band, i.e. a macrocrack, which comes into existence from the scattered network of microcracks at the onset of the softening, when the size of microstructural interaction domain is the largest. The highly non-linear softening model is embedded into the triangular C^1 finite element and implemented into the FE software ABAQUS via UEL subroutine.

The capabilities of the proposed computational strategy to simulate the strain localization are demonstrated in two benchmark examples in which the verification of the derived algorithm is performed by the comparison with the available solutions. Both homogeneous and heterogeneous materials are considered by employing the second-order homogenization procedure, mainly used in the multiscale computational approach, to obtain the required material stiffness matrices. It is observed that the damage response depends on the RVE size, porosity and average hole radius of the heterogeneous material. The structural responses clearly indicate that heterogeneous material has a much lower load-carrying capacity, as expected.

In contrast to the results obtained in the literature, where the conventional implicit gradient damage formulation is adopted, the proposed damage algorithm yields a fully localized deformation

band without any notice of spurious damage growth. The conducted analyses demonstrate that the proposed damage model based on the strain gradient continuum theory is able to successfully predict the initiation of the damage growth as well as to describe the subsequent localization of the deformation into a macroscopic crack, meaning that a complete regularization of the mathematical model of the material failure behavior can be achieved.

Acknowledgement

This work has been fully supported by Croatian Science Foundation under the project “Multiscale Numerical Modeling of Material Deformation Responses from Macro- to Nanolevel” (2516). The first author thanks Prof. M.G.D. Geers and Dr. R.H.J. Peerlings for valuable discussions during his stay at the Eindhoven University of Technology.

References

- Abaqus/Standard 6.13.4., 2013. Dassault Systemes, Simulia.
- Akarapu, S., Zbib, H.M., 2006. Numerical analysis of plane cracks in strain-gradient elastic materials. *Int. J. Fract.* 141, 403–430.
- Alshibli, K.A., Sture, S., 2000. Shear band formation in plane strain experiments of sand. *J. Geotech. Geoenviron. Eng.* 126, 495–503.
- Bažant, Z.P., Belytschko, T., Chang, T.P., 1984. Continuum theory for strain-softening. *J. Eng. Mech.* 110 (2), 666–1692.
- Bažant, Z.P., 1991. Why continuum damage is nonlocal: Micromechanics arguments. *J. Eng. Mech.* 117, 1070–1087.
- Chang, C.S., Ma, L., 1990. Modeling of discrete granulates as micropolar continua. *J. Eng. Mech.* 116 (12), 2703–2721.
- Chang, C.S., Askes, H., Sluys, L.J., 2002. Higher-order strain/higher-order stress gradient models derived from a discrete microstructure, with application to fracture. *Eng. Fract. Mech.* 69, 1907–1924.
- De Borst, R., Mühlhaus, H.B., 1992. Gradient-dependent plasticity: formulation and algorithmic aspects. *Int. J. Numer. Methods Eng.* 35, 21–39.
- De Borst, R., Sluys, L.J., Mühlhaus, H.B., Pamin, J., 1993. Fundamental issues in finite element analysis of localization of deformation. *Eng. Comput.* 10, 99–121.
- De Vree, J.H.P., Brekelmans, W.A.M., van Gils, M.A.J., 1995. Comparison of nonlocal approaches in continuum damage mechanics. *Comput. Struct.* 55, 581–588.
- Engelen, R.A.B., Geers, M.G.D., Baaijens, F.P.T., 2003. Nonlocal implicit gradient-enhanced elasto-plasticity for the modelling of softening behaviour. *Int. J. Plast.* 19, 403–433.
- Fischer, P., Mergheim, J., Steinmann, P., 2010. On the C^1 continuous discretization of non-linear gradient elasticity: a comparison of NEM and FEM based on Bernstein–Bézier patches. *Int. J. Numer. Methods Eng.* 82, 1282–1307.
- Forest, S., Trinh, D.K., 2011. Generalized continua and non-homogeneous boundary conditions in homogenisation methods. *ZAMM Z. Angew. Math. Mech.* 91, 90–109.
- Geers, M.G.D., de Borst, R., Brekelmans, W.A.M., Peerlings, R.H.J., 1998. Strain-based transient-gradient damage model for failure analyses. *Comput. Methods Appl. Mech. Eng.* 160, 133–153.
- Gitman, I.M., Askes, H., Sluys, L.J., 2007. Representative volume: existence and size determination. *Eng. Fract. Mech.* 74, 2518–2534.
- Kaczmarczyk, L., Pearce, C.J., Bičanić, N., 2008. Scale transition and enforcement of RVE boundary conditions in second-order computational homogenization. *Int. J. Numer. Methods Eng.* 74, 506–522.
- Kouznetsova, V.G., Geers, M.G.D., Brekelmans, W.A.M., 2002. Multi-scale constitutive modelling of heterogeneous materials with a gradient-enhanced computational homogenization scheme. *Int. J. Numer. Methods Eng.* 54, 1235–1260.
- Kouznetsova, V.G., Geers, M.G.D., Brekelmans, W.A.M., 2004. Size of a representative volume element in a second-order computational homogenization framework. *Int. J. Multiscale Comput. Eng.* 2 (4), 575–598.
- Lesičar, T., Tonković, Z., Sorić, J., 2014. A second-order two-scale homogenization procedure using C^1 macrolevel discretization. *Comput. Mech.* 54 (2), 425–441.
- Lesičar, T., Sorić, J., Tonković, Z., 2017. Two-scale computational approach using strain gradient theory at microlevel. *Int. J. Mech. Sci.* 126, 67–78.
- Li, J., 2011. A micromechanics-based strain gradient damage model for fracture prediction of brittle materials—part I: homogenization methodology and constitutive relations. *Int. J. Struct. Solids* 48, 3336–3345.
- Li, J., Zhang, X.B., 2013. A numerical approach for the establishment of strain gradient constitutive relations in periodic heterogeneous materials. *Eur. J. Mech. A/Solids* 41, 70–85.
- Mazars, J., Pijaudier-Cabot, G., 1989. Continuum damage theory—application to concrete. *J. Eng. Mech.* 115 (2), 345–365.
- Mindlin, R.D., 1965. Second gradient of strain and surface-tension in linear elasticity. *Int. J. Solids Struct.* 1, 417–438.
- Mindlin, R.D., Eshel, N.N., 1968. On first strain-gradient theories in linear elasticity. *Int. J. Solids Struct.* 4, 109–124.
- Nguyen, G.D., 2011. A damage model with evolving nonlocal interactions. *Int. J. Solids Struct.* 48, 1544–1559.

- Peerlings, R.H.J., de Borst, R., Brekelmans, W.A.M., de Vree, J.H.P., 1996. Gradient enhanced damage for quasi-brittle materials. *Int. J. Numer. Methods Eng.* 39, 3391–3404.
- Peerlings, R.H.J., de Borst, R., Brekelmans, W.A.M., Geers, M.G.D., 1998. Gradient-enhanced damage modelling of concrete fracture. *Mech. Cohesive-Frictional Mater.* 3, 323–342.
- Peerlings, R.H.J., 1999. Enhanced damage modeling for fracture and fatigue Ph.D. thesis. Eindhoven University of Technology, Netherlands.
- Pijaudier-Cabot, G., Haidar, K., Dube, J.F., 2004. Nonlocal damage model with evolving internal length. *Int. J. Numer. Anal. Methods Geomech.* 28, 633–652.
- Poh, L.H., Sun, G., 2017. Localizing gradient damage model with decreasing interactions. *Int. J. Numer. Methods Eng.* 110, 503–522. <http://dx.doi.org/10.1002/nme.5364>.
- Simone, A., Askes, H., Sluys, L.J., 2004. Incorrect initiation and propagation of failure in non-local and gradient enhanced media. *Int. J. Solids Struct.* 41, 351–363.
- Sluys, L.J., de Borst, R., 1992. Wave-propagation and localization in a rate-dependent cracked medium model formulation and one-dimensional examples. *Int. J. Solids Struct.* 29, 2945–2958.
- Sluys, L.J., de Borst, R., Mühlhaus, H.B., 1993. Wave propagation, localization and dispersion in a gradient-dependent medium. *Int. J. Solids Struct.* 30, 1153–1171.
- Triantafyllou, A., Perdikaris, P.C., Giannakopoulos, A.E., 2015. Gradient elastodamage model for quasi-brittle materials with an evolving internal length. *J. Eng. Mech.* 141, 04014139.
- Yang, Y., Misra, A., 2010. Higher-order stress-strain theory for damage modeling implemented in an element-free Galerkin formulation. *Comput. Model. Eng. Sci.* 64 (1), 1–36.
- Zervos, A., Papanicolopoulos, S.A., Vardoulakis, I., 2009. Two finite element discretizations for gradient elasticity. *J. Eng. Mech.* 135, 203–213.
- Zybell, L., Muehlich, U., Kuna, M., 2008. Constitutive equations for porous plane-strain gradient elasticity obtained by homogenization. *Arch. Appl. Mech.* 79 (4), 359–375.